Free wake panel method simulations of a highly flexible wing in flutter and gusts

Ribeiro, André F.P.; Casalino, Damiano; Ferreira, Carlos

DOI
10.1016/j.jfluidstructs.2023.103955

Publication date
2023

Document Version
Final published version

Published in
Journal of Fluids and Structures

Citation (APA)
Ribeiro, A. F. P., Casalino, D., & Ferreira, C. (2023). Free wake panel method simulations of a highly flexible wing in flutter and gusts. *Journal of Fluids and Structures*, *121*, Article 103955. https://doi.org/10.1016/j.jfluidstructs.2023.103955

Journal of Fluids and Structures 121 (2023) 103955

Contents lists available at ScienceDirect

Journal of Fluids and Structures

journal homepage: www.elsevier.com/locate/jfs

Free wake panel method simulations of a highly flexible wing in flutter and gusts

André F.P. Ribeiro *, Damiano Casalino, Carlos Ferreira

Faculty of Aerospace Engineering, Delft University of Technology, Kluyverweg 1, Delft, 2629 HS, Netherlands

ARTICLE INFO

Article history:
Received 13 December 2022
Received in revised form 16 May 2023
Accepted 7 July 2023
Available online xxxx

Keywords:
Fluid structure interaction
AePW
Large deflections
Pazy wing
Aeroelasticity

ABSTRACT

This paper presents low speed fluid structure interaction simulations of a highly flexible wing at various flow conditions, including flutter and excitation from sinusoidal gusts. Such wings are becoming more relevant in recent years, due to their potential for improving aerodynamics and reducing weight, while their flutter characteristics are particularly challenging to address, as the modal properties of the wings change as deflections increase. Calculations are based on time domain coupling of a geometrically exact beam structural model and a 3D free wake panel method, modeling the outer surface of the wing, which allow for nonlinear effects in terms of geometrical deformations and the flow at low computational cost. Static and aeroelastic wing deflections are in line with experimental data of the Pazy wing, which is a benchmark for highly flexible wings from Technion. Two flutter mechanisms are predicted within 1 to 3 m/s of the experimental range. An analysis of the flutter modes is performed, showing that the second torsion mode plays a role in flutter, something that had not been published before. Limit cycle oscillations are achieved and are shown to compare well with reference data, with the frequency being within 1% of the experimental value. Finally, results of gust simulations of the Pazy wing are compared to data from experiments and corrections for the wind tunnel measurements are proposed, which should facilitate future validation efforts. This work serves as a contribution to the Pazy wing dataset and is a step towards mid-fidelity simulations for more complex configurations.

1. Introduction

Aircraft wings have become more flexible in recent years, mostly due to high aspect ratio wings having favorable aerodynamic properties (such as lower induced drag) and lightweight structures helping improve fuel efficiency, but also because the flexibility of the wings can also have advantages for the dynamic response of the aircraft (Ritter and Hilger, 2022). These factors have led to the very flexible wings that are present in modern commercial aircraft such as the Boeing 787 and in high-altitude long-endurance drones. As wing deflections increase, the assumptions of linear models are no longer valid and nonlinear methods need to be used. As large deflections and rotations on wings change their aerodynamics and structural characteristics, nonlinear aeroelastic models and analysis methods are on the rise (Afonso et al., 2017). Models that can accurately include the large deflections into stability calculations of these wings at low computational cost are needed to avoid late stage modifications in the development cycle (Cesnik et al., 2014). In particular, the NASA Helios mishap led to the recommendation to develop more advanced multidisciplinary time domain methods appropriate for highly flexible aircraft (Noll et al., 2004).

* Corresponding author.
E-mail address: a.pintoribeiro@tudelft.nl (A.F.P. Ribeiro).

https://doi.org/10.1016/j.jfluidstructs.2023.103955

Nomenclature

CFD	Computational fluid dynamics
DLM	Doublet lattice method
FEM	Finite element method
VLM	Vortex lattice method
A	Area
A_G	Gust amplitude
$A_{G,\text{meas}}$	Measured gust amplitude
$A_{G,\infty}$	Freestream gust amplitude
A_{ij}	Doublets influence coefficient matrix
A_w	Tip displacement amplitude
B_{ij}	Sources influence coefficient matrix
C_{ij}	Wake vortices influence coefficient matrix
c	Wing chord
$c_{1,3,4}$	Lumped mass distance to node in the axial, vertical, and chordwise directions
d	Scalar distance along beam
$\vec{d}$	Direction of beam element
$\vec{F}$	Force vector
f_G	Gust frequency
G	Shear modulus
I	Inertia
K	Stiffness
m	Mass
n	Beam node
$\hat{n}$	Surface normal
s	Wing span
$\vec{s}$	Displacement vector
T	Gust period
$\vec{T}$	Torque vector
t	Time
$\vec{U_b}$	Body velocity vector
U_z	Vertical component of freestream velocity
U_∞	Freestream velocity
u	Displacement in x axis
w	Displacement in z axis
x	Streamwise direction
$\vec{x}$	Position vector
z	Vertical direction
α	Angle of attack
γ	Wake vortex strength
Δ	Difference between two quantities
Δt	Timestep
δW_a	Aerodynamic virtual work
δW_s	Structural virtual
θ	Rotation around y axis
$\vec{\theta}_s$	Beam node rotation vector
μ	Doublet strength
σ	Source strength
Φ	Velocity potential
Φ_∞	Freestream velocity potential
ϕ_G	Phase between wing tip displacement and gust vertical velocity

In order to validate such models, the Pazy wing experiment (Avin et al., 2022) was conducted as part of the Aeroelastic Prediction Workshop (AePW) Large Deflection Working Group (Ritter and Hilger, 2022; Drachinsky et al., 2022; Riso and Cesnik, 2023). The Pazy wing was created at Technion with the intent to be used for validation of aeroelastic models. It is a rectangular, flexible wing which exhibits two flutter modes. This provides a simple, yet challenging test case, as the wing deformation has substantial effects on its structural and aeroelastic properties, such as its modal characteristics, with "some trends that are opposite to those obtained in the linear domain" (Drachinsky and Raveh, 2021).

Several groups have simulated the Pazy wing, typically using nonlinear static and linearized dynamic simulations (Ritter et al., 2021), as adding both static and dynamic structural and aerodynamic nonlinearities concurrently is considered demanding (Righi, 2021). The linearization needs to be done on the deformed configuration, i.e., after statically deforming the wing for certain flow conditions, to deal with the wing static nonlinearities (Goizueta et al., 2022). High-fidelity, Navier–Stokes-based simulations using a detailed 3D structural model have the potential to perform such calculations in a structural and aerodynamic nonlinear framework (Fehrs et al., 2022), but the computational cost is still too high for the quick turnaround required during the design phase. The need to deform the volume mesh while supporting large deflections also complicates the use of methods that require off-body meshes.

Flexible wings can also go through large dynamic deformations outside of flutter, in the case of gusts. A modified version of the Pazy wing was constructed at the Delft University of Technology to perform wind tunnel analysis of its interactions with gusts (Mertens et al., 2023). This serves as an opportunity for validation of aeroelastic tools for the challenging case of sinusoidal gusts interacting with a highly flexible wing. To the authors knowledge, no numerical simulations of this configuration have been published.

Panel methods have shown good balance between accuracy and cost for the simulation of flexible wings (Yang et al., 2020). Typically, the vortex lattice method (VLM) or doublet lattice methods (DLM) are employed for aeroelastic simulations of wings (Patil and Hodges, 2004; Drachinsky and Raveh, 2021; Goizueta et al., 2022). These methods employ panel (doublet or vortex ring) sheets running through the wing chord line, hence thickness effects are neglected. A major drawback of using panel sheets is the difficulty in describing aircraft fuselages and other bodies that can have an effect on the wing aerodynamics, such as wing mounted pods.

An alternative to VLM and DLM is a full 3D panel method, where the complete surface of the aircraft is modeled. This allows for thickness effects to be captured, for boundary layer models to be included, and for a one-to-one correspondence with CFD results, in terms of surface data, so that corrections can be easily implemented in the panel code based on CFD simulations, which can capture transition effects and separations. Loads on fuselages can also be calculated more accurately, as their surfaces are represented. As VLM and DLM, full 3D panel methods are boundary element methods, and hence, only surface meshes are needed, simplifying the mesh deformation process.

VLM, DLM, and 3D panel methods simulations of wings can take several approaches to wake modeling (Katz and Plotkin, 2001). The most simple approach is a flat prescribed wake, aligned with the flow or trailing edge. This can be used to simulate steady cases quickly, without iterating on the wake position and its effects on the wing. Alternatively, the wake position can be partially defined, with the vertical locations of the points being changed through an iterative procedure (Maskew, 1987). For unsteady simulations, the wake can be either simply convected with the freestream velocity or the wake velocity can be computed, based on the freestream and the induction of the panels in the simulation (Katz and Plotkin, 2001). The latter approach is substantially more expensive, from a computational standpoint, but it allows for accurate wake motion and interactions (Gennaretti and Bernardini, 2007).

In this work, we seek to contribute to the Pazy wing studies and the AePW by conducting structurally and aerodynamically nonlinear, time domain simulations. We focus on validating a 3D panel code with free wake coupled with a geometrically exact beam structural model. These results are compared to experimental data and can serve as reference for future code verification. We also seek to contribute to the analysis of the flutter behavior of the Pazy wing, showing for the first time that the second torsion mode contributes to the first flutter mode of the wing. Finally, we conduct the first gust simulations of the Pazy wing and show that the gust properties measured in the experiments are strongly affected by the wing induction, which can help future validations with experimental data.

2. Numerical methods

2.1. Aerodynamics

We employ a source and doublet panel method with free-wakes (Katz and Plotkin, 2001) in order to capture the aerodynamics of the flexible wing. The code employed in this work was recently validated for moving airfoils and wind turbine rotors (Ribeiro et al., 2022). The thickness effects are fully captured, as the triangular or quadrilateral panels lie on the wing surface. The surface and wake discretizations of the velocity potential equation lead to the following:

$$\frac{1}{4\pi}A_{ij}\mu_j + \frac{1}{4\pi}B_{ij}\sigma_j + \frac{1}{4\pi}C_{iw}\gamma_w = 0 \tag{1}$$

where A_{ij}, B_{ij}, and C_{ij} are the influence coefficients matrices (Maskew, 1987) for the doublets μ, sources σ, and wake vortices γ respectively. This equation corresponds to the different contributions to the flow potential on the center a surface panel i, where there are contributions from all surface panels j and all wake panels w. The values of μ, σ, and γ

are constant over each panel. A far-field formulation can be used, which assumes that the distance between panels j or w to the center of panel i is constant over the area of the panels, meaning the dimensions of the panels are much smaller than the distance to the target. The formulation also assumes flat panels and makes the calculations of the influence coefficients substantially faster (Maskew, 1987). This far-field formulation can lead to issues with highly complex wakes (Ribeiro et al., 2022) where the wake panels are highly stretched and no longer flat, but it can be used for wings and we employ this in the current work.

The sources σ are computed to ensure impermeability, with:

$$\sigma = -(\vec{U}_\infty - \vec{U}_b) \cdot \hat{n} \tag{2}$$

where $\vec{U}_\infty$ is the freestream velocity, $\vec{U}_b$ is the local kinematic velocity of the panel, due to aeroelastic effects, and $\hat{n}$ is the surface normal. The wake vortices can be computed based on the potential on the top and bottom panels of the trailing edge, following the Kutta condition:

$$\gamma = \mu^{top} - \mu^{bottom} - (\Phi_\infty^{top} - \Phi_\infty^{bottom}) \tag{3}$$

where $\Phi_\infty = \vec{U}_\infty \cdot \vec{x}$ is the freestream potential at an arbitrary location $\vec{x}$, which in this case are the center of the top and bottom panels. The term in parentheses is often neglected, but is critical when simulating thick geometries using coarse meshes (Youngren et al., 1983), as the distance between the top and bottom panels are non-negligible. At every timestep, wake vortices are convected due to the freestream velocity and the induction of all the surface and wake panels. Wake-body interaction capabilities (Gennaretti and Bernardini, 2007) and a vortex core model (Ramasamy and Leishman, 2007) are implemented, but not used for this study, as the wake panels do not intersect the wing after they are released. Combining Eqs. (1), (2), and (3), we are left with a square linear system with the doublets μ as unknowns. We solve this system either by direct matrix inversion or by the generalized minimal residual method.

We employ virtual panels in order to simulate symmetry planes (Katz and Plotkin, 2001), which dramatically reduce the size of the influence coefficients matrices. With the linear system solved, surface velocities $\vec{U}$ are computed based on the basic potential flow equation, $\vec{U} = -\nabla\Phi$, where Φ is the velocity potential. The surface gradient is computed with central differences for quadrangular panels, but a least squares approximation (Anderson and Bonhaus, 1994; Sozer et al., 2014) is also available, and is always used for triangular panels. With the surface velocity available, the unsteady Bernoulli equation (Bernardini et al., 2013) is used to find the surface pressure, which is then integrated over all surface panels to find the forces and moments acting on the bodies. The time derivatives in the unsteady Bernoulli equation are calculated with a first order backwards Euler method, as is the value of $\vec{U}_b$, based on the position of the surface panels in the current and previous timesteps.

2.2. Structural model

The structural deformation of the wing is computed with a geometrically exact beam model, based on the works by Hodges (2006), Yu and Blair (2012), and Wang and Yu (2017). This allows for nonlinear, time domain calculations with large deflections, anisotropic deformation couplings, and curved beams. The open source Julia module GXBeam (McDonnell and Ning, 2022) is used with nonlinear time marching solutions for coupling to the aerodynamics solver, and for nonlinear engenvalue analysis for the initial validation of the wing vibration modes.

GXBeam was selected as the structural solver for three main reasons. First, it is written in Julia, as is the aerodynamics solver used for the simulations, which facilitates the coupling of the two codes. Second, it is a fast solver, being faster than the Fortran code GEBT (Yu and Blair, 2012) that GXBeam was originally based on. Lastly, it can simulate rotating structures composed of arbitrary numbers of connected composite beams in large deformations, which is not important for this work, but will be useful for aeroelastic simulation of wind turbines. GXBeam also supports automatic differentiation, has native support for unsteady adjoint sensitivity analysis, and performs rotation parameterization with an extension to Wiener–Milenković parameters, avoiding singularities (McDonnell, 2023). It uses the mixed variational formulation of geometrically exact beam theory (Hodges, 1990), which can avoid numerical integration if the lowest possible order shape functions are used.

Other similar open source geometrically exact beam models available are GEBT (Yu and Blair, 2012) and BeamDyn (Wang et al., 2017). Both codes are written in Fortran. GEBT is slower than GXBeam, and BeamDyn cannot handle beam assemblies, which is something that could be useful for simulating the Pazy with the tip rod and full wind turbines. GXBeam also has advantages over ASWING (Drela, 1999) in terms of solution smoothness (McDonnell, 2023). Validations and examples of GXBeam can be found in McDonnell (2022).

The structural properties of the beam model were computed based on a detailed 3D finite element method (FEM) wing model of the Pazy wing. The University of Michigan's process to convert 3D FEM models to beam models (Riso et al., 2020) was used and the beam model was then used by their Nonlinear Aeroelastic Simulation Toolbox (UM/NAST), originally developed by Su and Cesnik (2010). The beam has 16 equally spaced nodes, which was shown to be sufficient to capture the same modal behavior of the detailed FEM wing model (Riso and Cesnik, 2023). The elements are Timoshenko beams,

requiring 6×6 symmetric stiffness matrices:

$$\text{Stiffness Matrix} = \begin{bmatrix} K_{11} & 0 & 0 & K_{12} & K_{13} & K_{14} \\ 0 & GA & 0 & 0 & 0 & 0 \\ 0 & 0 & GA & 0 & 0 & 0 \\ K_{12} & 0 & 0 & K_{22} & K_{23} & K_{24} \\ K_{13} & 0 & 0 & K_{23} & K_{33} & K_{34} \\ K_{14} & 0 & 0 & K_{24} & K_{34} & K_{44} \end{bmatrix} \tag{4}$$

where K is the stiffness, the indices 1, 2, 3, and 4 correspond to the axial, torsion, out of plane bending (flapping), and in plane bending (horizontal, or edge-wise) displacements, G is the shear modulus, and A is the cross-section area. As done by Goizueta et al. (2022), we assume GA to be very large, as deflections due to shear are expected to be negligible compared to bending and torsion. Elements set to zero in the stiffness matrix are equivalent to no coupling between the shear and the beam axial, bending, and torsion deformations. The inertial effects are accounted for with 6×6 symmetric mass matrices. UM/NAST provided node-based mass matrices, defined as:

$$\text{Mass Matrix} = \begin{bmatrix} m & 0 & 0 & 0 & mc_3 & -mc_4 \\ 0 & m & 0 & -mc_3 & 0 & mc_1 \\ 0 & 0 & m & mc_4 & -mc_1 & 0 \\ 0 & -mc_3 & mc_4 & I_{22} & -I_{32} & I_{24} \\ mc_3 & 0 & -mc_1 & -I_{32} & I_{33} & -I_{34} \\ -mc_4 & mc_1 & 0 & I_{24} & -I_{34} & I_{44} \end{bmatrix} \tag{5}$$

where m is the lumped mass, i.e. the mass around the node that is modeled as concentrated on the node, c is the distance of the lumped mass to the beam node, as the nodes are not located in the section center of mass, and I the inertia, with indices consistent with the stiffness matrix.

2.3. Fluid structure interaction

A loosely-coupled approach (Bazilevs et al., 2013) for the aerodynamics and structural solvers is used to allow for fluid structure interaction (FSI) simulations. We now describe the coupling methods, which consist of a nearest neighbor method for converting the aerodynamic loads to the structural model and an orthogonal projection spline approach to convert the structural displacements to the aerodynamic panels.

Each surface panel i is associated with the nearest structural node j, which is part of a beam model. Then, the force acting on each panel $\vec{F}_i$ is added to the corresponding nodes. The torque associated with each force $\vec{T}_i = (\vec{x}_i - \vec{x}_j) \times \vec{F}_i$, where $\vec{x}_i$ is the panel center and $\vec{x}_j$ is the node coordinates vector, is also added to each node. These forces and torques are inputs to the structural solver, which in turn computes the displacement and rotation of each node of the beam model. Such point to point mapping is used successfully in wind turbine aeroelasticity (Sprague and Jonkman, 2014), although the nearest neighbor method does not conserve virtual work. Hence, we will verify the conservation of virtual work in this Section and the impact of the surface mesh in Section 4.3.

The geometry involved in the FSI coupling is shown in Fig. 1. Each structural node n_j has an associated direction $\vec{d}_j$, which is constructed as the difference between the next and previous nodes coordinates. Each surface vertex i is projected onto the beam by $d_i = (\vec{x}_i - \vec{x}_j) \cdot \vec{d}_j$, where d_i is the projected distance to the structural nodes. Splines (Dierckx, 1995) are constructed to interpolate the displacements and rotations along the beam element, so that smooth distributions are available along the span. Then, each surface point is rotated and translated around the beam model, based on those splines and assuming the cross-section to be rigid, which can also be interpreted as each cross section being rotated based on its projected distance d_i along the beam. This morphs the geometry into its new shape, while preserving a smooth panel distribution.

The influence coefficients are recomputed at every timestep, to account for relative motion between the panels. The main nonlinear effects that the current implementation neglects are related to flow separations, as the aerodynamic model is inviscid and hence unable to capture static or dynamic stall.

The current mapping scheme conserves total forces and moments, but does not ensure preservation of virtual work, due to the nearest neighbor interpolation. The error associated with this reduces with grid refinement. We can calculate the virtual work δW_a performed by the aerodynamic forces $\vec{F}$, based on the displacement of the surface panels $\vec{s}$:

$$\delta W_a = \sum_i \vec{F}_i \cdot \vec{s}_i \tag{6}$$

where the sum is performed over all surface panels i. We can also calculate the virtual work δW_s performed by the structural forces $\vec{F}$ and torques $\vec{T}$, based on the associated displacements $\vec{s}$ and rotations $\vec{\theta}$:

$$\delta W_s = \sum_j \vec{F}_j \cdot \vec{s}_j + \sum_j \vec{T}_j \cdot \vec{\theta}_j \tag{7}$$

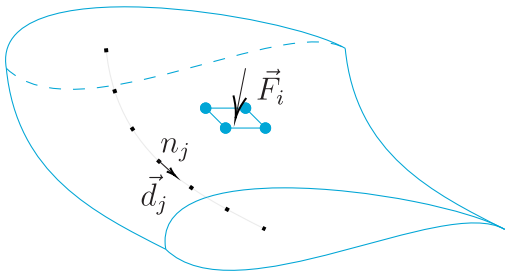

Fig. 1. Example of an aerodynamic section and panel (in blue) and the beam model nodes (black). (For interpretation of the references to color in this figure legend, the reader is referred to the web version of this article.)

where the sum is performed over all beam nodes j. In our simulations, the differences between δW_a and δW_s were typically well under 1% for most cases and around 2% for extreme cases, near the second flutter mode. Hence, we consider the current model appropriate for this work.

3. Test case description

The Pazy wing (Avin et al., 2022) is a highly flexible wing constructed at Technion specifically for validation of aeroelastic models. It is a simple cantilevered rectangular wing composed of a NACA0018 airfoil with chord $c = 0.1$ m and span $s = 0.558$ m (which could also be referred to as the semispan). Tip deflections of approximately half of the span were reached in the experiments. Limit cycle oscillations (LCO) were encountered and measured in the experiments. They are caused by flutter involving the second out of plane bending mode and first torsion mode at relatively low speeds, while higher speeds develop flutter with the first out of plane bending mode and first torsion mode. Both flutter modes occur at high wing deflections, meaning linearized dynamics methods must be used only after nonlinear static deflections, as at such deformation levels, influence coefficients need to be recomputed. The second flutter mode is difficult to reach experimentally without damaging the wing.

The wing skin, which is made of polyester shrink film, introduces pre-tension, deforming between the ribs. It also buckles at large wing deformations, adding some uncertainty to the aerodynamics of the wing and structural properties of the skin. While many simulations of the Pazy wing are computed using the structural model of the wing with and without the skin, as a way to estimate the experimental uncertainty (Goizueta et al., 2022), we focus on the experimental data with skin only. It is worth noting that given a stable and accurate 3D FEM model that could provide a very detailed surface geometry of the wing with the deformed skin, the 3D panel method used in this work could include the aerodynamic effects of the buckling, keeping in mind the limitations of the inviscid approach. Such a model is not available for the Pazy wing at the moment.

We model the Pazy wing using quadrilateral panels, with 150 panels in the chordwise direction with a cosine distribution (refining the leading and trailing edges), and 26 panels in the spanwise direction, with a uniform distribution. The surface mesh is shown in Fig. 2, along with the coordinate system definition used in this work. A symmetry plane is placed on the wing root to model the wind tunnel wall, mirroring the wing surface and wake panels. The timestep is set to $\Delta t = 0.25c/U_\infty$. The spanwise panel discretization and the timestep length are verified in Section 4.3. Wake panels are deleted once they reach the arbitrary location of $x = 10$ s, as this saves computational time and does not affect the results noticeably. Simulations are run for at least 2000 timesteps, or 500 flow passes, where the first 4 timesteps are used to initialize the wake, with a rigid wing. Detecting the presence of flutter could be done early in the simulation, as will be shown in Section 4.2.

4. Results

4.1. Structural model validation

We start by verifying and validating the structural model without the aerodynamics. The experimental data set includes static wing deformation, achieved by placing a weight at the wing tip. Two cases are investigated: with the weight applied near the elastic center, and with a lever arm of 0.13 m, dubbed the bend and the torsion tests, respectively. The wing tip vertical displacement w is shown in Fig. 3, corresponding to the bend test. Note that the wing was built slightly bent, leading to a tip displacement of 18.8 mm at the tip even with zero tip mass, which we applied in the structural model. Gravity forces were applied o the corresponding lumped masses. The wing tip twist θ from the torsion test is shown in Fig. 4. Reference data for the beam model computed by DLR are shown for the bend test. Throughout this work, the wing displacement and θ are measured in beam node location, which is at 44% of the wing chord. Here, we measure θ by projecting the tip leading and trailing edges on a vertical plane, to approximate how it was done experimentally.

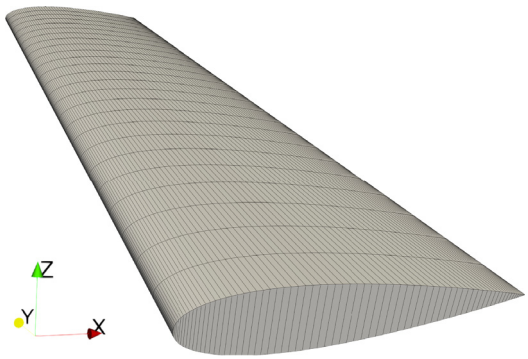

Fig. 2. Surface mesh of the Pazy wing, seen from the root side.

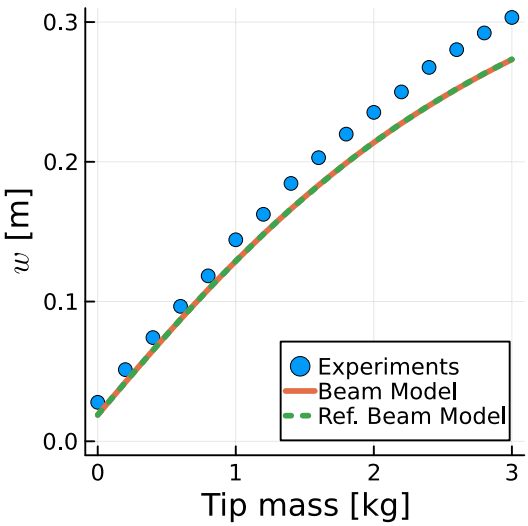

Fig. 3. Static wing bend test results. Vertical tip displacement versus mass placed at wing tip.

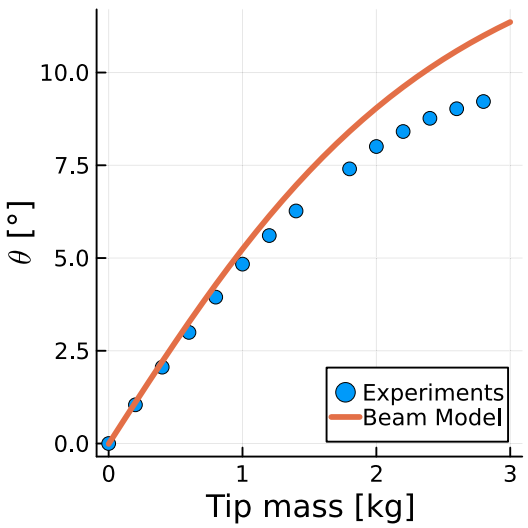

Fig. 4. Static wing torsion test results. Tip twist angle versus mass placed at wing tip, behind the trailing edge.

Table 1
Natural frequencies (Hz) of the undeformed wing beam model.

Mode	Description	Current results	UM/NAST	Δ
1	1st bending	4.19	4.19	<0.1%
2	2nd bending	28.50	28.49	<0.1%
3	1st torsion	42.02	41.88	0.3%
4	3rd bending	83.11	83.06	<0.1%
5	1st horizontal	105.23	105.89	0.6%

Displacements are almost indistinguishable from the reference beam results, with discrepancies up to about 15% with experimental data for high values of tip mass. In the experiments, the skin of the wing buckled and behaved in a nonlinear way for large deflections, something the beam model does not capture. The twist behaves in a similar fashion, but with discrepancies closer to 20% for higher mass, with some uncertainty associated with twist angles for large values of w, as measuring the twist is more difficult to do with large deflections, since the wing cross section is no longer aligned with the horizontal axis. Overall we consider the results verified, as they reproduce the reference beam model, which is the most accurate geometrically nonlinear numerical representation available for the Pazy wing with skin, and agree with data shown in Riso and Cesnik (2023), which indicate the beam model is being used correctly. In terms of validation with the experiments, at the moment we are not aware of a more accurate structural representation of the Pazy wing (the FEM with skin fails in nonlinear solutions), hence while the agreement could be improved, it seems to be at the state-of-the-art.

The natural frequencies of the undeformed model are shown in Table 1, where "bending" stands for the out of plane bending mode and "horizontal" stands for the in plane bending mode. The frequencies are compared with UM/NAST results (Riso and Cesnik, 2023), using the same stiffness and inertia matrices for the beam model used in this work. The two codes agree very well, providing confidence in the structural model used in this work. The difference between the current results and UM/NAST is shown in the Δ column, and is typically under 0.1%.

4.2. Aeroelastic simulations validation

The Pazy flutter boundaries were measured by recent experiments (Drachinsky et al., 2022) where two instability regions could be extracted: a smaller onset region and a larger offset region. For example, at static root angle of attack $\alpha = 3°$, if the flow speed was continuously increased, the wing would start vibrating at 49 m/s. Once the vibrations started, a hysteresis effect would mean that decelerating to 40 m/s was required to stop them. The onset region matched numerical predictions (Drachinsky and Raveh, 2021; Riso and Cesnik, 2022) very well, which we will discuss in Section 4.5. These results correspond to the first flutter region, which is a hump mode that involves the first torsion and second bending modes. Increasing the flow speed made the vibrations disappear. At much higher flow speeds, a second flutter region appears, involving the first torsion and first bending modes. The experimental flutter boundary for the second flutter region is not yet available, hence numerical data is used for reference.

Aeroelastic simulations were conducted for $\alpha = 3$, 5, and 7°, with U_∞ up to 80 m/s. Figs. 5 and 6 show the time history of the wing tip twist angle θ for four simulations at different U_∞ and $\alpha = 3°$. At $U_\infty = 45$ and 75 m/s, oscillations appear early in the simulations ($tU_\infty/c = 100$), but they are damped and θ ultimately converges to a steady value. For $U_\infty = 50$ m/s, θ diverges as the wing encounters the first flutter mode. The same happens at $U_\infty = 80$ m/s for the second flutter mode. Oscillations for the second flutter mode clearly occur at much lower frequencies and higher amplitudes than the first, as the second flutter mode is linked to the first bending mode. Note that from here on, θ is simply the angle around the spanwise direction, or y axis, as computed by the structural model, hence without a projection to a vertical plane.

Fig. 7 shows the vertical tip displacement of the wing w as a function of the freestream velocity U_∞ for $\alpha = 3$, 5, and 7°. The blue diamonds represent the experimental first flutter onset region, i.e., the velocities in which the wing enters flutter. The area shaded in blue represents the experimental first flutter speed range, that is, once the wing starts to flutter, it needs to go outside that range of U_∞ for flutter to stop. The velocities at the edge of this range are the flutter offset velocities. Note that for $\alpha = 7°$ there was no experimental data for reducing U_∞, hence the upper range of the flutter onset and lower range of the flutter offset are unknown. The dashed blue lines represent the experimental static deformation of the wing. The green diamonds show the second flutter onset region found with SHARPy (Goizueta et al., 2022) for the Pre-Pazy wing, which is slightly different from the Pazy wing simulated here, but serves as the best current estimate of the second flutter onset. The orange circles represent simulations with the present panel method, while the stars highlight cases for which the simulations led to large vibrations, as shown in Figs. 5 and 6.

The current results in Fig. 7 are in line with the references. A quantitative comparison with the static deformation results is difficult to perform, as there are errors associated to those measurements, especially at low velocities, due to the wing being slightly bent and twisted. Qualitatively, results agree well. The numerical flutter range is within 1 m/s of the experimental flutter onset range for $\alpha = 3$ and 7° and within 3 m/s for $\alpha = 5°$. The second flutter onset points match the SHARPy results within 1 m/s. In this Section, the objective was to find the conditions that create flutter, rather than

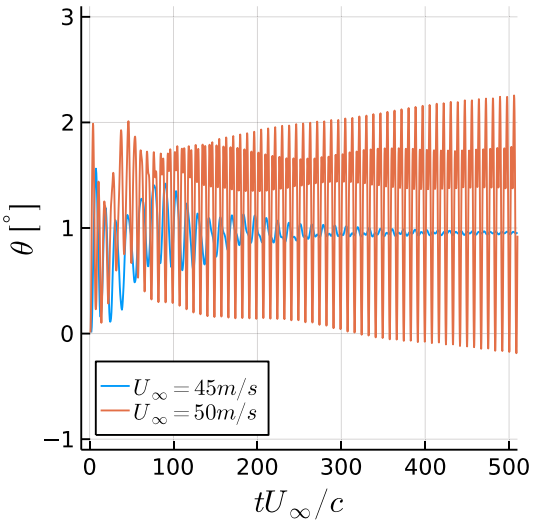

Fig. 5. Time history of wing tip twist for $\alpha = 3°$ near and at the first flutter mode. (For interpretation of the references to color in this figure legend, the reader is referred to the web version of this article.)

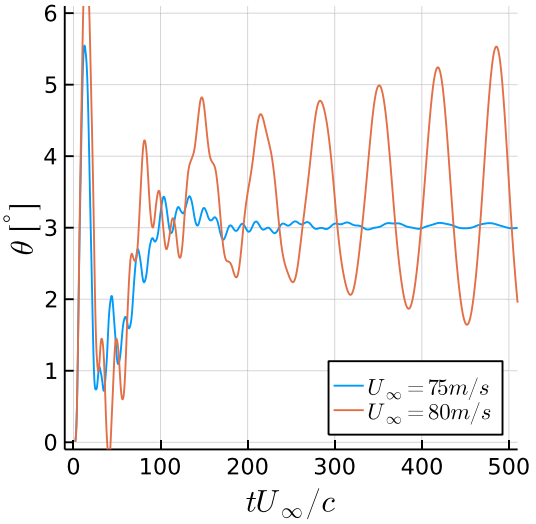

Fig. 6. Time history of wing tip twist for $\alpha = 3°$ near and at the second flutter mode. (For interpretation of the references to color in this figure legend, the reader is referred to the web version of this article.)

trying to characterize the LCO, which will be done in Section 4.5. Hence, the simulations here were run until it was clear that the fluctuations were growing, not until LCO was reached.

Note that in this Section we scale our velocities to better compare to experiments. Based on the dynamic pressure and velocities stated in Avin et al. (2022), the fluid density in the experiments can be induced to be 1.19 kg/m^3, while our simulations and the ones by Goizueta et al. (2022) use 1.225 kg/m^3. Hence, we scale all simulation velocities in this Section by $\sqrt{1.19/1.225}$, so that the same dynamic pressures can be compared.

4.3. Resolution study

In order to verify that our aerodynamic surface mesh and timestep are adequate for our simulations, we perform resolution studies. The chordwise panel distribution of our aerodynamic surface mesh is consistent with previous studies (Ribeiro et al., 2022) and will not be examined in this work. However, the spanwise discretization can be an important factor, as it influences interpolation mapping between the aerodynamic and structural models. Hence, we test two surface meshes in this Section: the baseline mesh with 26 spanwise sections, and a fine mesh with 39 spanwise sections. The refinement ratio of 1.5 between the two meshes was chosen because it is large enough to show potential

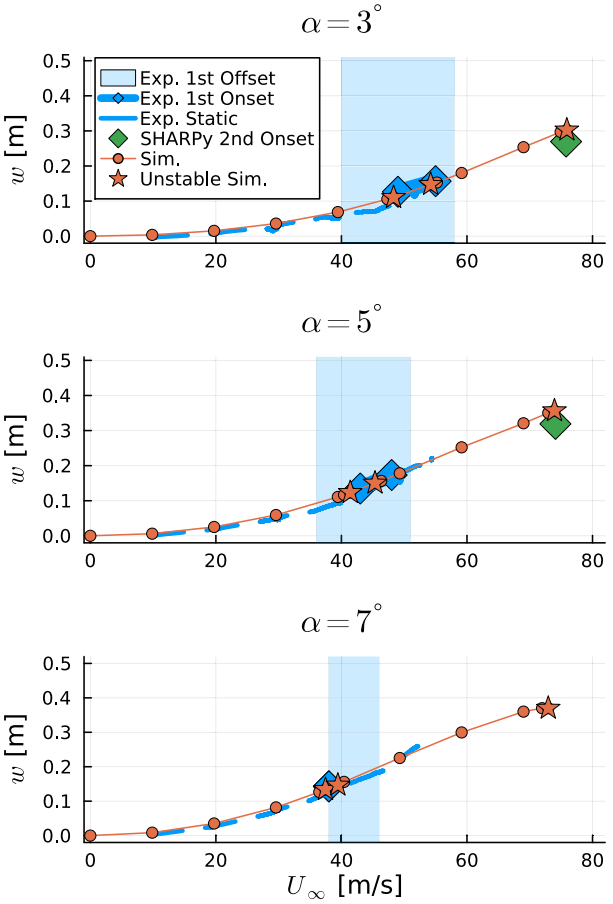

Fig. 7. Vertical tip displacement for various flow velocities at three angles of attack. (For interpretation of the references to color in this figure legend, the reader is referred to the web version of this article.)

differences, while forcing the spanwise discretization to be different from the baseline case, whereas a refinement ratio of 2 would have kept half of the spanwise panel nodes to be in the same position as in the baseline. The fine mesh simulations took approximately 70% more computational time than the baseline simulations.

For determining if the timestep is adequate for our simulations, we compare the baseline simulations with timestep $\Delta t = 0.25c/U_\infty$ with two additional simulations with timesteps $2\Delta t$ and $\Delta t/2$. This changes the computational cost by a substantial amount for two reasons: first, halfing the timestep means the number of timesteps in a simulation need to be doubled to achieve the same physical time. Second, halfing the timestep doubles the number of wake panels present during the simulation. The first leads to a simple linear behavior, doubling the simulation time, while the latter doubles the number of some of the calculations, such as the induction from the surface panels on the wake panels, but increases with $O(N^2)$ the number of calculations on the wake interacting with itself. This made the simulations about three times faster for $2\Delta t$ and over three times more expensive for $\Delta t/2$.

We use the simulations at $\alpha = 5^\circ$ and simulate the points before and after the first flutter mode, and before the second flutter mode. This is done to check if the wing tip displacements are consistent for a wide range of flow velocities. Results are shown in Fig. 8.

Fine mesh results are within 0.6% of the baseline results, indicating the discretization is appropriate for the mapping and subsequent coupling between the aerodynamic and structural models. Differences in tip displacement for the cases with doubled and halved timesteps are well within 0.05% of the baseline results, indicating the timestep used in the simulations is adequate. We now turn to the flutter onset itself. We simulate the different cases at intervals of 1 m/s near the first and second flutter modes, to determine the flutter range for each case. Results are shown in Table 2. Results are given with the simulation fluid density and hence should be scaled in order to compare to experiments.

Given our step in velocities of 1 m/s, the spanwise resolution does not affect the flutter velocities on its own. The largest timestep modifies the 1st flutter start speed by 1 m/s, but otherwise all results are identical. The reason we use the baseline timestep instead of the largest timestep used here is that the largest timestep was unable to achieve LCO. This will be further discussed in Section 4.5.

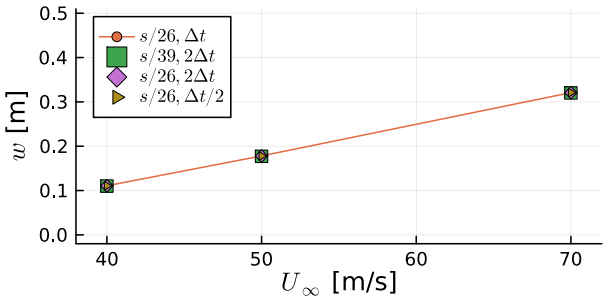

Fig. 8. Vertical tip displacement for various flow velocities at $\alpha = 5°$. Baseline surface mesh, spanwise refined surface mesh, and simulations where the timestep is doubled and halved.

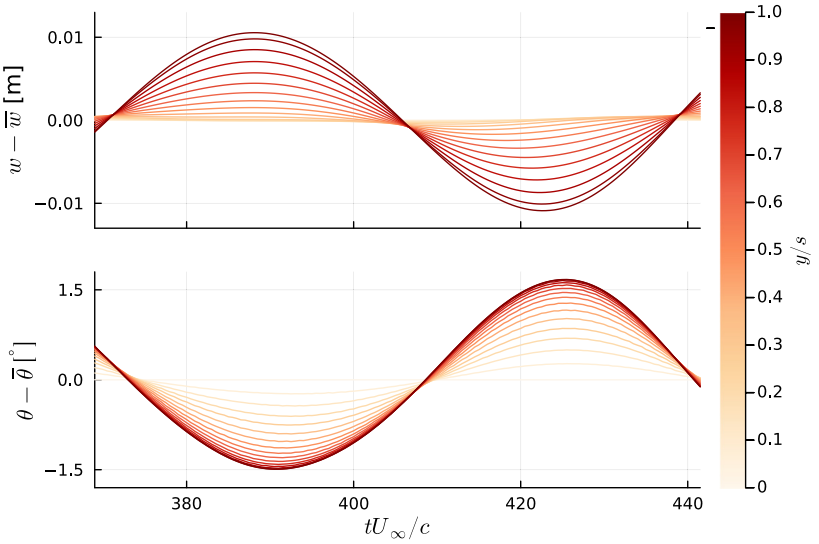

Fig. 9. Vertical displacement fluctuation along the wing (top), and twist angle fluctuation along the wing (bottom) for $\alpha = 3°$, $U_\infty = 80$ m/s, at the second flutter mode. Colors represent the spanwise position. (For interpretation of the references to color in this figure legend, the reader is referred to the web version of this article.)

Table 2
Flutter speeds in m/s at $\alpha = 5°$. Cases with different spanwise resolutions and timesteps. Fluid density is 1.225 kg/m^3.

Panels/span	Timestep factor	1st start	1st end	2nd start
26	1/2	42	46	75
26	1	42	46	75
26	2	43	46	75
39	2	43	46	75

With the tip deformation results and the flutter speeds showing very little effects from spanwise refinement and timestep changes, we consider the resolution study conducted in this Section sufficient to give us confidence in results using the baseline spanwise resolution of 26 panels per span and the timestep of $\Delta t = 0.25c/U_\infty$.

4.4. Flutter characteristics

We turn our attention to two specific cases of the previous section: $U_\infty = 50$ and 80 m/s at $\alpha = 3°$. These cases produced the first and second flutter modes of the Pazy wing, respectively. We seek to characterize the flutter motion in Figs. 9 and 10. The second flutter mode, shown in Fig. 9 is displaying a vertical displacement that is in opposite phase with the wing twist, while being about 15° ahead of it. The entire wing is bending and twisting in the same direction, indicating this is indeed a combination of the first bending and first twisting modes.

Fig. 10 shows the same analysis on the first flutter mode. Consistent with the experimental analysis (Drachinsky et al., 2022), the vertical displacement (which is changing signs around 85% of the span) corresponds to the second bending

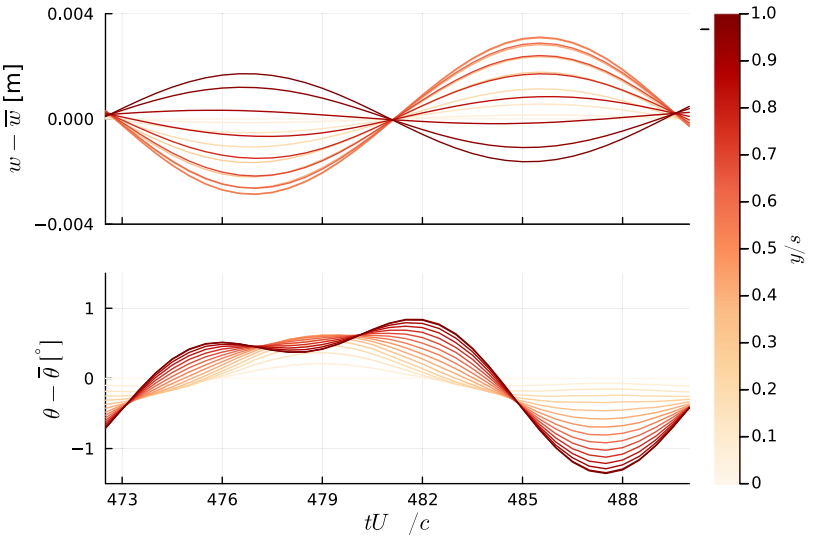

Fig. 10. Vertical displacement fluctuation along the wing (top), and twist angle fluctuation along the wing (bottom) for $\alpha = 3°$, $U_\infty = 50$ m/s, at the first flutter mode. Colors represent the spanwise position. (For interpretation of the references to color in this figure legend, the reader is referred to the web version of this article.)

mode and is in phase with the twist, and about 50° ahead of it (as evidenced by the trough for $w - \bar{w}$ near $tU_\infty/c = 486$ and the trough for $\theta - \bar{\theta}$ at $tU_\infty/c = 487$).

The second torsion mode seems to be present in the results, as seen by the θ curves. The structural model for this case was not validated for the second torsion mode, hence it is not obvious if this mode is correct or not. Similar curves from experimental data (Drachinsky et al., 2022) show wiggles that could be due to the second torsion mode, but could also be noise from the measurements. The presence of this mode might be correct, as simulations using linearized models that require the eigenmodes as inputs have shown that including the second torsion mode was important for accuracy (Ritter, 2022). Also, experiments have shown that three sine waves are needed to represent the strain on the wing at LCO, which could indicate the presence of three modes (Drachinsky et al., 2022).

The Pazy wing, along with its wake, is shown in Figs. 11 and 12 for the first and second flutter modes, respectively. The wakes are colored by the vortex strength γ, which is proportional to the sectional circulation, and hence, lift coefficient, at the time the wake panel is shed. The second flutter mode, shown in Fig. 12, occurs at very large levels of wing deformation. White regions on the wake indicate high sectional lift and we can see two white spots, one near the wing and one at 60% of the wake length, showing the low frequency of the wing oscillations. The first flutter mode, on Fig. 11, is clearly occurring at a much higher frequency. As the second bending mode is active, the color patterns on the wake are more complex, as the lift along the wing is not fluctuating in a synchronized fashion. We can also observe the wake structures becoming larger and more complex as they move downstream, as one would expect from a plunging airfoil (Young and Lai, 2004).

4.5. Limit cycle oscillations

LCO refer to the oscillations of a vibrating system that have stabilized to a somewhat periodic behavior. Predicting the LCO response of a highly flexible wing introduces significant challenges on top of the flutter onset prediction. Not only must the flutter onset be accurately captured, but nonlinear mechanisms that limit the oscillations are required to avoid divergence.

Two types of flutter LCO are possible in flutter: supercritical and subcritical (Marzocca et al., 2002; Dowell et al., 2003). In supercritical LCO, the oscillations appear at a certain flow speed (the flutter speed) and progressively increase as the speed increases. The oscillations disappear as the flow speed is brought back to the flutter speed. In subcritical LCO, flutter is more abrupt and large oscillations appear as soon as the flutter speed is reached. The flow speed must then be reduced to a value lower than the original flutter speed for the oscillations to disappear. Hence, hysteresis effects play an important role in the flutter offset.

Critically, flow separation, which can at times have a stabilizing role, in the sense that it can reduce the forces acting on the wing, can have a destabilizing role in flutter, leading to subcritical LCO (Dowell et al., 2003). For the Pazy wing, the first flutter mode clearly shows subcritical behavior in the experiments. Simulations that do not include flow separation, but include geometric nonlinear effects have been shown to capture the amplitude of the LCO associated with the first flutter mode of the Pazy wing (Riso and Cesnik, 2022), but not the subcritical effects. In the case of the present simulations,

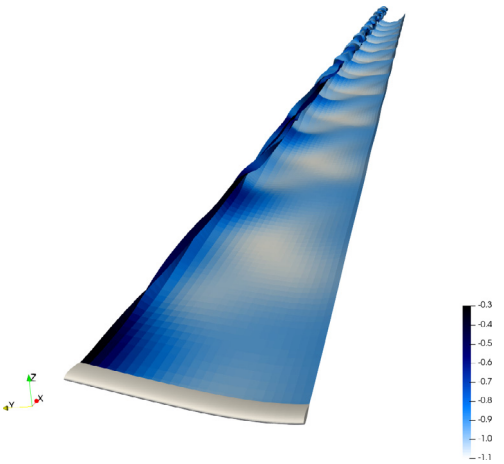

Fig. 11. Pazy wing and its wake, colored by vortex strength, at $\alpha = 3°$, $U_\infty = 50$ m/s. First flutter mode. (For interpretation of the references to color in this figure legend, the reader is referred to the web version of this article.)

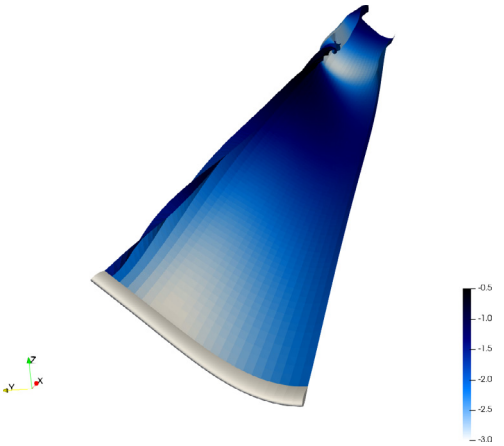

Fig. 12. Pazy wing and its wake, colored by vortex strength, at $\alpha = 3°$, $U_\infty = 80$ m/s. Second flutter mode. (For interpretation of the references to color in this figure legend, the reader is referred to the web version of this article.)

nonlinear geometry effects come from the structural model, while nonlinear inviscid aerodynamic effects (Ribeiro et al., 2023), come from the panel code. Flow separation is missing, meaning capturing the subcritical LCO is likely not possible, but achieving LCO for the first flutter mode should be.

For the second flutter mode, above 70 m/s, we were not able to stabilize the simulations, as flutter initiates quickly and the oscillations are large, leading to numerical instabilities in the solution. For the first flutter mode, achieving a stable solution was possible, as long as we use a timestep $\Delta t = 0.25c/U_\infty$ or lower. Doubling the timestep led to numerical instabilities.

We believe the reason for these instabilities at larger timesteps is that the larger timestep was not able to accurately represent the second torsion mode. The second torsion mode has a period of about $8c/U_\infty$, meaning the larger timestep was resolving it with 16 points per oscillation. Previous studies on plunging airfoils (Ribeiro et al., 2022) have shown that a phase error of $O(5°)$ is made when using 20 timesteps per periods for reduced frequencies near 0.4 (which is the reduced frequency of the Pazy wing for the second torsion mode at the flow conditions for the first flutter mode). Using the smaller timesteps, the second torsion had half the period of the first torsion mode, making them synchronized throughout the simulations and reducing the θ peak in Fig. 10. With the larger timestep, the second torsion mode was not synchronized with the first torsion mode and eventually they had a constructive interference effect, making the θ peak even higher, leading to large deflections that would make the structural solver unstable.

Results for the LCO achieved with $\Delta t = 0.25c/U_\infty$ are shown in Fig. 13. The original run time of 500 flow passes has to be extended to about 1200 flow passes to quantify LCO. In this Section, our results are at $\alpha = 3°$ and $U_\infty = 50$ m/s. The first flutter mode LCO frequency for the Pazy wing shows little variation with α and U_∞ (Drachinsky et al., 2022) and is between 25 and 30 Hz. Previous simulations (Ritter and Hilger, 2022) found a similar range, between 31 and 33 Hz.

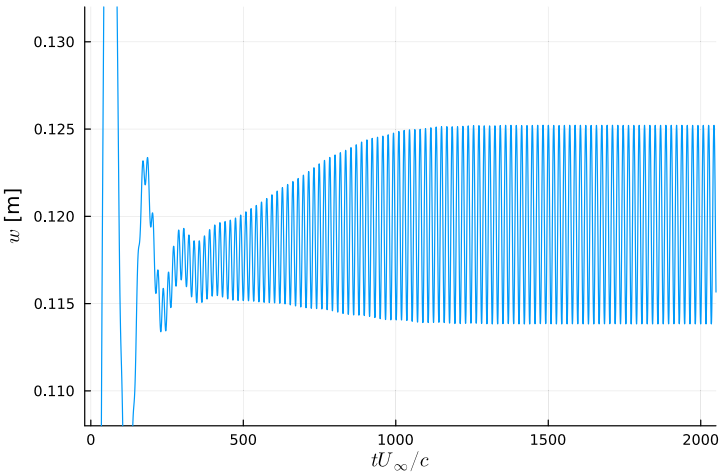

Fig. 13. Time history of wing tip displacement for $\alpha = 3°$, $U_\infty = 50$ m/s.

Table 3
Experimental conditions of the gust cases.

Case	α (°)	f_G (Hz)	A_G (m/s)
1	5	5.7	0.81
2	10	3.2	0.65

Our current results indicate LCO at 28.5 Hz, while the experiments show around 28.3 Hz at $\alpha = 3°$ and $U_\infty = 50$ m/s, making this an excellent agreement, within under 1%. The amplitude of the tip displacements was found to be about 2% of the span, which is in line with other numerical results (Riso and Cesnik, 2022). The LCO amplitude also seems to have only small variations with α and U_∞.

4.6. Gust interaction

A modified version of the Pazy wing, the Delft-Pazy wing, was experimentally tested with gusts at the Delft University of Technology (Mertens et al., 2023). This wing was made more flexible, to allow for large deflection under lower wind velocities. Externally, the wing is almost identical to the Technion built Pazy wing. The beam model developed by the University of Michigan for the original Pazy wing was updated to account for the lower stiffness of the Delft-Pazy wing (Riso, 2022), meaning a methodology identical to the one used in the previous sections can be applied to the Delft-Pazy wing.

Wind tunnel data are available for sinusoidal gusts interacting with the wing for two cases. The vertical velocity of the gust follows the form:

$$U_z(t) = A_G \sin(2\pi f_G t) \tag{8}$$

where U_z is the vertical component of the freestream velocity, A_G is the gust amplitude, f_G is the gust frequency, and t is time. The spanwise freestream velocity is zero and streamwise component of the freestream velocity can be adjusted to achieve a constant velocity magnitude of $U_\infty = 18.3$ m/s.

One of the advantages of the current panel method is that the freestream velocity can be an arbitrary user defined function, whereas CFD methods could smear sharp gusts before they reach the target object, due to numerical diffusion. For this case, this means we can create gusts that are functions of time and space, which for the Delft-Pazy wing corresponds to:

$$U_z(x, t) = A_G \sin\left(2\pi f_G \frac{U_\infty t - x}{U_\infty}\right) \tag{9}$$

where x is the streamwise coordinate. Here we have a gust that at a given instant in time has a wavelength of U_∞/f_G that is convected with U_∞.

The results of these gust experiments are tip deflections, defined as $w = \bar{w} + A_w sin(2\pi f_G + \phi_w)$, where A_w is the amplitude of the tip deflection motion and ϕ_w is the phase between the tip deflection and the gust velocity at the wing root quarter chord location. The two test conditions from the experiments of Mertens et al. (2023) are shown in Table 3. Here, α is the steady mean angle of attack of the wing root.

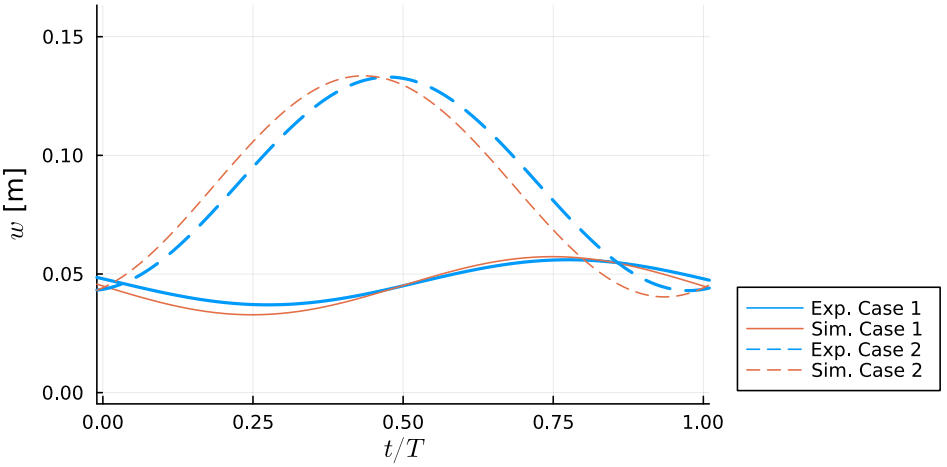

Fig. 14. Vertical tip displacement of the Delft-Pazy wing under gusts. (For interpretation of the references to color in this figure legend, the reader is referred to the web version of this article.)

Table 4
Case 1 results for experiments, simulations, and simulations with corrected gust.

	Exp.	Sim.	Δ	Sim. corr.	Δ
$A_{G,\infty}$ (m/s)	–	0.81	–	0.69	–
$A_{G,\text{meas}}$ (m/s)	0.81	0.96	19%	0.81	0%
$\bar{w}$ (m)	0.0465	0.0451	−3%	0.0450	−3%
A_w (m)	0.0095	0.0123	29%	0.0104	10%
ϕ_G (°)	–	0	–	6	–
ϕ_w (°)	171	180	9°	174	3°

The wing tip deflection for simulations and experiments over a gust period $T = 1/f_G$ for cases 1 and 2 are shown in Fig. 14. Note that T is different for cases 1 and 2. The amplitudes of the tip displacement are over predicted (19% for case 1) and the phase difference is larger than expected (15° for case 2). The present method has been shown to capture amplitude and phase of moving geometries (Ribeiro et al., 2022) and it should be accurate for the present case, barring low Reynolds effects being dominant. We believe there are two main reasons for the discrepancies. The first is that experiments measured the gust $0.75c$ upstream of the wing center span and assumed negligible unsteady influence of the wing on the measurement location. The second is the assumption that the gust travels with U_∞ near the wing, ignoring the flow deceleration near the stagnation point. Both points could affect the amplitude and phase of the wing response.

The second point can be addressed by directly including the guide vanes of the wing tunnel in the simulations (Kassem, 2019), which is beyond the scope of our work. The first can be addressed by using the present simulations to estimate the effect of the wing on the measurement. Another advantage of the present method is the potential to break down the velocity in a point in space into the freestream component and the induction by arbitrary sets of surface and wake panels. Hence, we measured the wing induction on the same location as the experiments. This location was a plane $0.75c$ upstream the unrotated wing leading edge, at spanwise coordinates 140 to 415 mm, where zero spanwise coordinate corresponds to the wing root, and transverse coordinates −80 to 140 mm for case 1, −60 to 160 mm for case 2, where a zero transverse coordinate is at the chord line. The wing was then rotated around its mid point, to achieve the correct angle of attack. The planes for cases 1 and 2 are shown in Fig. 15.

With these measurements, we can compare the measured $A_{G,\text{meas}}$ with the freestream $A_{G,\infty}$, which in the experiments were assumed to be the same. The objective is to achieve an $A_{G,\text{meas}}$ close to the experimental value by correcting $A_{G,\infty}$, which is unknown in the experiments. We can also check if there is a phase between the imposed and measured gust, ϕ_G, caused by the wing induction. The results of this study are summarized in Tables 4 and 5. The difference Δ is always relative to the experimental value. For case 1 the wing deflection is smaller, putting it closer to the measurement plane. A freestream gust of 0.69 m/s leads to the measured gust of 0.81 m/s. Correcting for the gust amplitude does not change ϕ_w, but the wing introduces a phase error in the measurement plane of $\phi_G = 6°$, which can be used as a correction. For case 2 the wing is more deflected and hence further away from the measurement plane, leading to smaller effects of the wing on the measurement plane. The large phase differences for case 2 could be explained by the trailing edge separations on the wing seen in experiments (Mertens et al., 2023).

The corrections obtained in this study improved wing tip displacement correlations with experimental data by only using the flow velocities achieved in the simulations on the measurement plane. It is worth noting that, in the experiments,

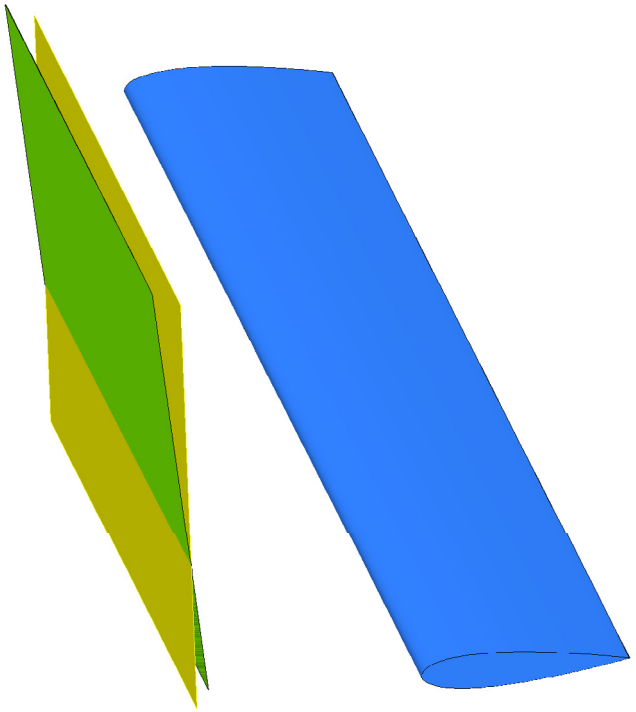

Fig. 15. Delft-Pazy wing (blue), along with the experimental measurement planes for cases 1 (yellow) and 2 (green). (For interpretation of the references to color in this figure legend, the reader is referred to the web version of this article.)

Table 5
Case 2 results for experiments, simulations, and simulations with corrected gust.

	Exp.	Sim.	Δ	Sim. corr.	Δ
$A_{G,\infty}$ (m/s)	–	0.65	–	0.62	–
$A_{G,\text{meas}}$ (m/s)	0.65	0.69	6%	0.65	0%
$\bar{w}$ (m)	0.088	0.086	−2%	0.087	−2%
A_w (m)	0.045	0.046	2%	0.044	−2%
ϕ_G (°)	–	0	–	2	–
ϕ_w (°)	−81	−66	15°	−68	13°

the gusts were generated using guide vanes which oscillated in angle of attack. The amplitude of these oscillations was 5° for cases 1 and 2, meaning that A_G was expected to be quite similar for both cases, being different only due to the effects of changing f_G. Hence, the corrected values of $A_{G,\infty}$ of 0.69 and 0.62 m/s are more in line with expectations than the original wind tunnel values of 0.81 and 0.65 m/s.

5. Conclusions and outlook

Simulations of the highly flexible Pazy wing were conducted for different angles of attack and flow velocities. The structural model and the aeroelastic simulations were compared with experimental data, with good agreement being found. In particular, the flutter onset was predicted within 1 m/s of the experimental values for most angles of attack. No artificial displacement or velocity was applied to the wing for it to start vibrating in the simulations. These are the first published results for the Pazy wing using a time domain 3D panel method with a free wake.

An analysis of the flutter motion was done, in order to clarify the phenomena occurring at the first and second flutter modes. We found that the first flutter mode includes the second torsion mode of the wing. As described in Section 4.4, we have reasons to believe this is correct and, to our knowledge, this is the first time this behavior was clearly identified and documented. Previous publications describe the first flutter region of the Pazy wing as a combination of the first torsion mode and the second bending mode only. We also show that by reducing the timestep in the simulation, LCO were obtained for the first flutter mode, with the LCO frequency being within 1% of the experimental data.

Simulations of the wing under gusts were also conducted and validated with experimental data. To our knowledge, this work shows the first numerical validation of the Delft-Pazy wing gust experiments. It was shown that errors in amplitude and phase were related to the wing induction at the experimental measurement location. In the experiments,

it was assumed that the wing induced a constant velocity at the measurement location and with our method we can isolate that effect from the incoming gust. We demonstrated that the current method can be used to correct this measurement error, leading the simulations to show a substantially better agreement with the tip displacement amplitude seen in the experiments. In the presence of flow separations, the current method loses accuracy and comparisons to experiments are less reliable.

The framework developed herein can be applied to other, more complex cases in the future, where the advantages of a full 3D panel method would be more evident. Such cases can include fuselage-mounted wings, wings with pods, or aircraft where the wing wake has strong interactions with the horizontal tail plane.

Each case simulated herein (i.e., each angle of attack and flow speed combination) was run in about 30 min on a desktop with 20 cores. This was sufficient to determine the shape of the wing and if flutter took place. Using the larger timestep, which produced results within 1 m/s of the baseline results for flutter onset, but could not achieve LCO, the run time was reduced to 5 min. In order to quantity the LCO, simulations with baseline timestep took about 70 min. Hence, the current methods are a fraction of the cost of CFD, but substantially more expensive than linearized methods. These run times can be reduced in the future by code and setup optimization. Changes that could substantially reduce the run time are: reducing the length of the wake, coarsening the surface mesh, increasing the timestep (as demonstrated), updating the influence coefficient matrices less often, and skipping the calculation of the wake velocity, letting it convect with the freestream.

Future simulations of the Pazy wing with the current method can include more geometrical details, such as the wing tip rod, and the deformed wing skin. A detailed structural model, including the deformation of the wing skin could be developed in the future and coupled with aerodynamic simulations. Such a model is not yet available, as knowing the structural properties of the skin is challenging, as is modeling its buckling. More analysis of the second flutter mode can also be done, as doing so experimentally has been difficult, due to the high dynamic pressures and deformations that can damage the wing. Finally, the guide vanes in the wind tunnel could be included to more accurately model the gust response.

Declaration of competing interest

The authors declare that they have no known competing financial interests or personal relationships that could have appeared to influence the work reported in this paper.

Data availability

Data will be made available on request

Acknowledgments

The authors are grateful to Markus Ritter and Arik Drachinsky of the AePW Large Deflections Working Group, for their valuable feedback and assistance. We also acknowledge the help of Philipp Drescher and Daniella Raveh, for providing the reference beam results and information on the Pazy wing, respectively. We thank Cristina Riso for the beam model structural properties. We are also grateful to Christoph Mertens for the Delft-Pazy wind tunnel data and discussions on the gust results. The structural solver used in this work is GXBeam and we are thankful to Taylor McDonnell, its developer, for support in its use.

References

Afonso, F., Vale, J., Oliveira, E., Lau, F., Suleman, A., 2017. A review on non-linear aeroelasticity of high aspect-ratio wings. Prog. Aerosp. Sci. 89, 40–57. http://dx.doi.org/10.1016/j.paerosci.2016.12.004.

Anderson, W.K., Bonhaus, D.L., 1994. An implicit upwind algorithm for computing turbulent flows on unstructured grids. Comput. & Fluids 23 (1), 1–21. http://dx.doi.org/10.1016/0045-7930(94)90023-X.

Avin, O., Raveh, D.E., Drachinsky, A., Ben-Shmuel, Y., Tur, M., 2022. Experimental aeroelastic benchmark of a very flexible wing. AIAA J. 60 (3), 1745–1768. http://dx.doi.org/10.2514/1.J060621.

Bazilevs, Y., Takizawa, K., Tezduyar, T.E., 2013. Computational Fluid-Structure Interaction: Methods and Applications. John Wiley & Sons.

Bernardini, G., Serafini, J., Molica Colella, M., Gennaretti, M., 2013. Analysis of a structural-aerodynamic fully-coupled formulation for aeroelastic response of rotorcraft. Aerosp. Sci. Technol. 29 (1), 175–184, URL: https://doi.org/10.1016/j.ast.2013.03.002.

Cesnik, C.E., Palacios, R., Reichenbach, E.Y., 2014. Reexamined structural design procedures for very flexible aircraft. J. Aircr. 51 (5), 1580–1591. http://dx.doi.org/10.2514/1.C032464.

Dierckx, P., 1995. Curve and surface fitting with splines. In: Monographs on Numerical Analysis. Clarendon Press, URL: https://books.google.com/books?id=-RIQ3SR0sZMC.

Dowell, E., Edwards, J., Strganac, T., 2003. Nonlinear aeroelasticity. J. Aircr. 40 (5), 857–874. http://dx.doi.org/10.2514/2.6876.

Drachinsky, A., Avin, O., Raveh, D.E., Ben-Shmuel, Y., Tur, M., 2022. Flutter tests of the Pazy wing. AIAA J. 60 (9), 5414–5421. http://dx.doi.org/10.2514/1.J061717.

Drachinsky, A., Raveh, D.E., 2021. Nonlinear aeroelastic analysis of highly flexible wings using the modal rotation method. AIAA J. 60 (5), 3122–3134. http://dx.doi.org/10.2514/1.J061065.

Drela, M., 1999. Integrated simulation model for preliminary aerodynamic, structural, and control-law design of aircraft. In: 40th Structures, Structural Dynamics, and Materials Conference and Exhibit. http://dx.doi.org/10.2514/6.1999-1394.

Fehrs, M., Ritter, M., Helm, S., Mertens, C., 2022. CFD simulations of the Pazy wing in support of the third aeroelastic prediction workshop. In: International Forum on Aeroelasticity and Structural Dynamics (IFASD).
Gennaretti, M., Bernardini, G., 2007. Novel boundary integral formulation for blade-vortex interaction aerodynamics of helicopter rotors. AIAA J. 45 (6), 1169–1176. http://dx.doi.org/10.2514/1.18383.
Goizueta, N., Wynn, A., Palacios, R., Drachinsky, A., Raveh, D.E., 2022. Flutter predictions for very flexible wing wind tunnel test. J. Aircr. 59 (4), 1082–1097. http://dx.doi.org/10.2514/1.C036710.
Hodges, D.H., 1990. A mixed variational formulation based on exact intrinsic equations for dynamics of moving beams. Int. J. Solids Struct. 26 (11), 1253–1273. http://dx.doi.org/10.1016/0020-7683(90)90060-9.
Hodges, D., 2006. Nonlinear Composite Beam Theory. In: Progress in Astronautics and A, American Institute of Aeronautics and Astronautics, URL: https://books.google.com/books?id=FEFKAQAAIAAJ.
Kassem, A.V., 2019. Wind Gust Generation for Wind Turbine Testing Via Numerical Methods (Master's thesis). Delft University of Technology, URL: http://resolver.tudelft.nl/uuid:38f8aab2-cfed-4568-97da-f3677f777fe8.
Katz, J., Plotkin, A., 2001. Low-Speed Aerodynamics, second ed. In: Cambridge Aerospace Series, Cambridge University Press, http://dx.doi.org/10.1017/CBO9780511810329.
Marzocca, P., Librescu, L., Silva, W.A., 2002. Flutter, postflutter, and control of a supersonic wing section. J. Guid. Control Dyn. 25 (5), 962–970. http://dx.doi.org/10.2514/2.4970.
Maskew, B., 1987. Program VSAERO Theory Document: A Computer Program for Calculating Nonlinear Aerodynamic Characteristics of Arbitrary Configurations. Contractor Report 4023, National Aeronautics and Space Administration, URL: https://ntrs.nasa.gov/citations/19900004884.
McDonnell, T., 2022. GXBeam.jl. https://github.com/byuflowlab/GXBeam.jl, Accessed: October 4 2022.
McDonnell, T.G., 2023. Gradient-Based Optimization of Highly Flexible Aeroelastic Structures (Ph.D. thesis). URL: https://scholarsarchive.byu.edu/etd/9907, Accessed: October 4 2022.
McDonnell, T., Ning, A., 2022. GXBeam: A pure Julia implementation of geometrically exact beam theory. J. Open Source Softw. 7 (73), 3997. http://dx.doi.org/10.21105/joss.03997.
Mertens, C., Costa Fernández, J.L., Sodja, J., Sciacchitano, A., van Oudheusden, B.W., 2023. Nonintrusive experimental aeroelastic analysis of a highly flexible wing. AIAA J. 61 (4), http://dx.doi.org/10.2514/1.J062476.
Noll, T.E., Brown, J.M., Perez-Davis, M.E., Ishmael, S.D., Tiffany, G.C., Gaier, M., 2004. Investigation of the Helios Prototype Aircraft Mishap. Volume I. Mishap report, https://www.nasa.gov/pdf/64317main_helios.pdf, Accessed: May 10 2023.
Patil, M., Hodges, D., 2004. On the importance of aerodynamic and structural geometrical nonlinearities in aeroelastic behavior of high-aspect-ratio wings. J. Fluids Struct. 19 (7), 905–915. http://dx.doi.org/10.1016/j.jfluidstructs.2004.04.012.
Ramasamy, M., Leishman, J.G., 2007. A Reynolds number-based blade tip vortex model. J. Am. Helicopter Soc. 52 (3), 214–223. http://dx.doi.org/10.4050/JAHS.52.214.
Ribeiro, A.F.P., Casalino, D., Ferreira, C.S., 2022. Surging wind turbine simulations with a free wake panel method. J. Phys. Conf. Ser. 2265 (4), 042027. http://dx.doi.org/10.1088/1742-6596/2265/4/042027.
Ribeiro, A.F.P., Casalino, D., Ferreira, C.S., 2023. Nonlinear inviscid aerodynamics of a wind turbine rotor in surge, sway, and yaw motions using a free-wake panel method. Wind Energy Sci. 8 (4), 661–675. http://dx.doi.org/10.5194/wes-8-661-2023.
Righi, M., 2021. Uncertainties quantification in flutter prediction of a wind tunnel model exhibiting large displacements. In: AIAA Scitech Forum. http://dx.doi.org/10.2514/6.2021-1037.
Riso, C., (2022). AePW3-LDWG, https://github.com/UM-A2SRL/AePW3-LDWG, Accessed: October 4 2022.
Riso, C., Cesnik, C.E., 2022. Post-flutter dynamics of the Pazy wing geometrically nonlinear benchmark model. In: International Forum on Aeroelasticity and Structural Dynamics (IFASD).
Riso, C., Cesnik, C.E.S., 2023. Impact of low-order modeling on aeroelastic predictions for very flexible wings. J. Aircr. 60 (2), http://dx.doi.org/10.2514/1.C036869.
Riso, C., Sanghi, D., Cesnik, C.E., Vetrano, F., Teufel, P., 2020. Parametric roll maneuverability analysis of a high-aspect-ratio-wing civil transport aircraft. In: AIAA Scitech 2020 Forum. http://dx.doi.org/10.2514/6.2020-1191.
Ritter, M., (2022). October 13, Personal communication.
Ritter, M., Hilger, J., 2022. Dynamic aeroelastic simulations of the Pazy wing by UVLM with nonlinear viscous corrections. In: AIAA SCITECH 2022 Forum. http://dx.doi.org/10.2514/6.2022-0177.
Ritter, M., Hilger, J., Zimmer, M., 2021. Static and dynamic simulations of the Pazy wing aeroelastic benchmark by nonlinear potential aerodynamics and detailed FE model. In: AIAA Scitech Forum. http://dx.doi.org/10.2514/6.2021-1713.
Sozer, E., Brehm, C., Kiris, C.C., 2014. Gradient calculation methods on arbitrary polyhedral unstructured meshes for cell-centered CFD solvers. In: 52nd Aerospace Sciences Meeting. AIAA, http://dx.doi.org/10.2514/6.2014-1440.
Sprague, M.A., Jonkman, J.M., 2014. FAST modular wind turbine CAE tool: Nonmatching spatial and temporal meshes. In: 32nd ASME Wind Energy Symposium. http://dx.doi.org/10.2514/6.2014-0520.
Su, W., Cesnik, C.E.S., 2010. Nonlinear aeroelasticity of a very flexible blended-wing-body aircraft. J. Aircr. 47 (5), 1539–1553. http://dx.doi.org/10.2514/1.47317.
Wang, Q., Sprague, M.A., Jonkman, J., Johnson, N., Jonkman, B., 2017. BeamDyn: a high-fidelity wind turbine blade solver in the FAST modular framework. Wind Energy 20 (8), 1439–1462. http://dx.doi.org/10.1002/we.2101.
Wang, Q., Yu, W., 2017. Geometrically nonlinear analysis of composite beams using Wiener-Milenković parameters. J. Renew. Sustain. Energy 9 (3), 033306. http://dx.doi.org/10.1063/1.4985091.
Yang, L., Xie, C., Yang, C., 2020. Geometrically exact vortex lattice and panel methods in static aeroelasticity of very flexible wing. Proc. Inst. Mech. Eng. G 234 (3), 742–759. http://dx.doi.org/10.1177/0954410019885238.
Young, J., Lai, J.C.S., 2004. Oscillation frequency and amplitude effects on the wake of a plunging airfoil. AIAA J. 42 (10), 2042–2052. http://dx.doi.org/10.2514/1.5070.
Youngren, H., Bouchard, E., Coopersmith, R., Miranda, L., 1983. Comparison of panel method formulations and its influence on the development of QUADPAN, an advanced low-order method. In: Applied Aerodynamics Conference. URL: https://doi.org/10.2514/6.1983-1827.
Yu, W., Blair, M., 2012. GEBT: A general-purpose nonlinear analysis tool for composite beams. Compos. Struct. 94 (9), 2677–2689. http://dx.doi.org/10.1016/j.compstruct.2012.04.007.